Structural and magnetic investigation of the interfaces of Fe_3O_4/MgO(001) with and without NiO interlayer

Tobias Pohlmann,[1,2] Florian Bertram,[1] Jannis Thien,[2] Jari Rodewald,[2] Kevin Ruwisch,[2] Timo Kuschel,[3] Eugen Weschke,[4] Karsten Küpper,[2] and Joachim Wollschläger[2,*]

[1]*Deutsches Elektronen-Synchrotron DESY, Notkestrasse 85, 22607 Hamburg, Germany*

[2]*Department of Physics, Osnabrück University, Barbarastrasse 7, 49076 Osnabrück, Germany*

[3]*Center for Spinelectronic Materials and Devices, Department of Physics, Bielefeld University, Universitätsstrasse 25, 33615 Bielefeld, Germany*

[4]*Helmholtz-Zentrum Berlin für Materialien und Energie, Wilhelm-Conrad-Röntgen-Campus BESSY II, Albert-Einstein-Strasse 15, 12489 Berlin, Germany*

(Received 5 December 2021; revised 4 April 2022; accepted 1 June 2022; published 27 June 2022)

We present an investigation on the structural and magnetic properties of the interfaces of Fe_3O_4/MgO(001) and Fe_3O_4/NiO/MgO(001) by extracting cation-selective magneto-optical depth profiles by means of x-ray resonant magnetic reflectivity in combination with charge-transfer multiplet simulations of x-ray magnetic circular dichroism data. For Fe_3O_4/MgO(001), the magneto-optical depth profiles at the Fe^{2+}_{oct} and the Fe^{3+}_{oct} resonant energies follow exactly the structural profile, while the magneto-optical depth profile at the Fe^{3+}_{tet} resonance is offset by 3.2 ± 1.3 Å from the interface, consistent with a *B*-site interface termination of Fe_3O_4 with fully intact magnetic order. In contrast, for Fe_3O_4/NiO(001), the magneto-optical depth profiles at the Fe^{2+}_{oct} and the Ni^{2+} resonances agree with the structural profile, but the interface positions of the magneto-optical depth profiles at the Fe^{3+}_{oct} and the Fe^{3+}_{tet} resonances are spatially shifted by 3.3 ± 1.4 and 2.7 ± 0.9 Å, respectively, not consistent with a magnetically ordered stoichiometric interface. This may be related to an intermixed (Ni, Fe)O layer at the interface. The dichroic depth profile at the Ni L_3 edge might hint at uncompensated magnetic moments throughout the NiO film.

DOI: 10.1103/PhysRevB.105.235436

I. INTRODUCTION

Magnetite (Fe_3O_4) is a half-metallic ferrimagnet in the inverse spinel structure. This structure consists of a cubic close-packed oxygen lattice whose interstitial sites are populated by three different iron species: 1/2 of the octahedral *B* sites are occupied randomly by divalent Fe^{2+}_{oct} and trivalent Fe^{3+}_{oct} cations, and 1/8 of the tetrahedral *A* sites are occupied by trivalent Fe^{3+}_{tet} cations. The two octahedrally coordinated species Fe^{2+}_{oct} and Fe^{3+}_{oct} are ferromagnetically coupled by double exchange, while the Fe^{3+}_{oct} and Fe^{3+}_{tet} cations couple antiferromagnetically via superexchange. Therefore, the magnetic moments of the Fe^{3+} cations compensate each other and the resulting macroscopic moment of Fe_3O_4 of 4.07 μ_B/f.u. is determined by the magnetic moments of the Fe^{2+}_{oct} cations [1].

Due to these magnetic properties, magnetite is a long-standing candidate to contribute to all-oxide thin-film spintronic devices, as a source for spin-polarized currents [2–7]. These kinds of devices utilize the fact that many metal oxides with varying electronic and magnetic properties grow in spinel or rocksalt structures, such as the conducting ferrimagnets Fe_3O_4 and γ-Fe_2O_3, the insulating ferrimagnets $NiFe_2O_4$ and $CoFe_2O_4$, the insulating antiferromagnets NiO, CoO, and FeO, or the insulating diamagnets MgO and $MgAl_2O_4$, which all share a cubic close-packed oxygen lattice with very similar lattice constants [2]. This allows epitaxial growth of film stacks with a large variety of spin electronic functionality but with little strain and thus supposedly well-matching interfaces.

However, a drawback of this concept is that the structural similarity of these metal oxides also means that undesired modifications at their interfaces are difficult to detect, such as interdiffusion of Mg [8], Ni [9,10], or Co [11] into Fe_3O_4 films, or the transformation of the different iron oxides into each other [12,13]. All-oxide spintronic devices with Fe_3O_4 electrodes indeed did not prove to be very successful yet; their shortcomings were speculated to stem from magnetic dead layers at the substrate interface [14,15] or other interface effects [7].

Of particular interest have been the interfaces between Fe_3O_4 films and the tunnel barrier material MgO [7,15,16], as well as the interface between Fe_3O_4 and antiferromagnetic films, e.g., NiO, exhibiting exchange bias [17–20]. This effect can cause a shift of the coercive fields of the ferrimagnetic Fe_3O_4 film and be used to pin its magnetization state.

In this paper, we investigate the structural and magnetic properties of the Fe_3O_4/NiO and Fe_3O_4/MgO interfaces. We grow Fe_3O_4 single layers and Fe_3O_4/NiO bilayers on MgO(001) by reactive molecular beam epitaxy (RMBE) and investigate the distribution and magnetic order of the

*jwollsch@uni-osnabrueck.de

three cations Fe^{2+}_{oct}, Fe^{3+}_{tet}, and Fe^{3+}_{oct} of Fe_3O_4 and of the Ni^{2+} cations of NiO by x-ray resonant magnetic reflectivity (XRMR) combined with a charge-transfer multiplet analysis of x-ray magnetic circular dichroism (XMCD) spectra. We find that the magnetic structure of Fe_3O_4 on MgO is intact down to the interface, while on the Fe_3O_4/NiO interface the data indicate a disturbed magnetic order. XRMR data on the Ni L_3 edge indicate uncompensated magnetic moments in the antiferromagnet NiO.

II. EXPERIMENTAL DETAILS

The deposition and characterization methods of the samples followed the ones presented in Refs. [10,20]. We prepared Fe_3O_4/MgO(001) and Fe_3O_4/NiO/MgO(001) samples in a multichamber ultrahigh-vacuum system with a base pressure of $p_0 < 1 \times 10^{-8}$ mbar. Before deposition, the MgO(001) substrates were annealed at 400 °C in an oxygen atmosphere of 1×10^{-4} mbar for 1 h. Our films were grown by RMBE. For the NiO, we deposited nickel in an oxygen pressure of 1×10^{-5} mbar, and for the Fe_3O_4, we deposited iron in an oxygen pressure of 5×10^{-6} mbar. We limited the substrate temperature to 250 °C in order to avoid interdiffusion of Mg into the films [8]. After growth, the electronic structures of the films were characterized *in situ* by x-ray photoelectron spectroscopy (XPS) using a Phoibos HSA 150 hemispherical analyzer and an Al $K\alpha$ anode, and their surface structure by low-energy electron diffraction (LEED). The Fe $2p$ XPS spectra show the Fe^{2+} and the Fe^{3+} features typical for Fe_3O_4, and the LEED patterns confirm the characteristic $(\sqrt{2} \times \sqrt{2})R45°$ surface structure of Fe_3O_4 [21,22] (both not shown here).

Fe_3O_4/MgO(001) and Fe_3O_4/NiO/MgO(001) samples were transported under ambient conditions to BESSY II for x-ray absorption spectroscopy (XAS), XMCD, x-ray reflectivity (XRR), and XRMR studies on the XUV diffractometer at beamline UE46_PGM-1 [23]. The samples were placed between two permanent magnets in a magnetic field of 200 mT at room temperature, resulting in a degree of magnetization of about 85% of saturation magnetization. The x rays had a degree of 90% circular polarization.

All XAS and XMCD spectra were recorded in total electron yield (TEY) mode with an incidence glancing angle of 30°. XRR and XRMR curves were obtained by θ-2θ scans in the range $2\theta = 0°$–$140°$ at selected resonant photon energies with both right and left circularly polarized x rays. The structural properties of the films (thickness d, roughness σ) obtained by XRR at an off-resonant energy (1000 eV, cf. Fig. 1) are summarized in Table I.

In order to obtain magnetic information with higher depth sensitivity, we measured XAS and XMCD in total fluorescence yield mode (TFY) and reflection mode on a different Fe_3O_4/NiO/MgO sample at the Diamond Light Source (DLS), on the RASOR diffractometer of beamline I10. A sample of higher film thicknesses was chosen for these measurements in order to increase the TFY signal. It was placed in a similar magnet setup, again in a magnetic field of 200 mT and at room temperature. Here, the x rays had a degree of circular polarization of 99%. The structural properties of this sample can be found in Table I too.

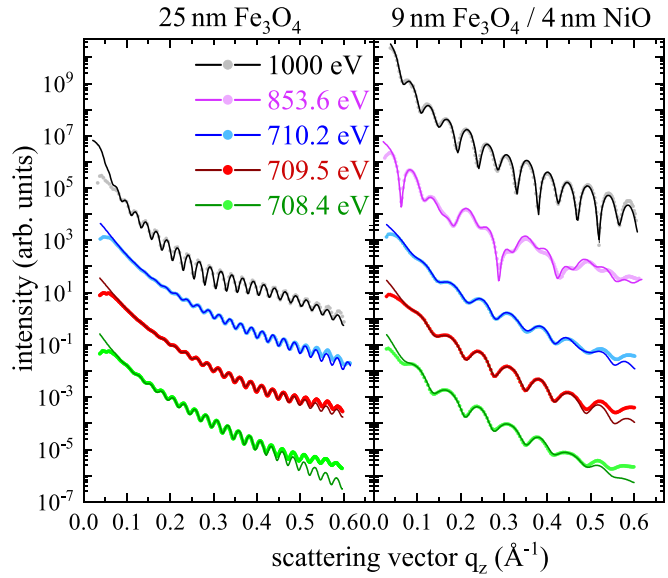

FIG. 1. XRR measurements of the two samples recorded at the three resonant energies of the Fe L_3 XMCD spectrum of Fe_3O_4 (708.4, 709.5, 710.2 eV), the energy of the Ni L_3 maximum (853.6 eV), and at an off-resonant energy (1000 eV). The q_z range shown corresponds to an angular range of $2\theta = 0°$–$115°$.

III. DATA ANALYSIS

A. XMCD

To obtain cation- and lattice-site-selective magneto-optical depth profiles, first the XMCD spectra have to be analyzed. Figures 2(a) and (b) show exemplarily XAS and XMCD spectra, respectively, of the Fe $L_{2,3}$ edges of the Fe_3O_4/NiO/MgO sample. The XAS spectrum has been obtained as the sum, the XMCD spectrum as the difference of the absorption spectra recorded with left and right polarized x rays,

$$\mathrm{XAS} = \mathrm{XAS}^{\mathrm{left}} + \mathrm{XAS}^{\mathrm{right}}, \tag{1}$$

$$\mathrm{XMCD} = \mathrm{XAS}^{\mathrm{left}} - \mathrm{XAS}^{\mathrm{right}}, \tag{2}$$

with the maximum of the XAS curve normalized to 1. Charge-transfer multiplet calculations of the three Fe cations of Fe_3O_4 using the THOLE code [24] with the assistance of CTM4XAS [25,26] provide the three individual XAS and XMCD spectra shown below the data. For these calculations, we used

TABLE I. Film thicknesses d_i and rms roughnesses σ_i of the three investigated samples, obtained from off-resonant XRR measurements recorded at 1000 eV. Corresponding data and fits for the UE46_PGM-1 samples are shown in Fig. 1.

	BESSY II UE46_PGM-1		DLS I10
	Fe_3O_4/MgO	Fe_3O_4/NiO/MgO	Fe_3O_4/NiO/MgO
$d_{Fe_3O_4}$	25.2 ± 0.3 nm	9.3 ± 0.1 nm	17.6 ± 0.1 nm
d_{NiO}		4.3 ± 0.1 nm	27.3 ± 0.2 nm
$\sigma_{Fe_3O_4}$	3.3 ± 0.5 Å	3.2 ± 0.5 Å	2.0 ± 0.6 Å
σ_{NiO}		3.0 ± 0.2 Å	4.2 ± 0.8 Å
σ_{MgO}	3.5 ± 0.5 Å	2.7 ± 0.5 Å	2.5 ± 0.3 Å

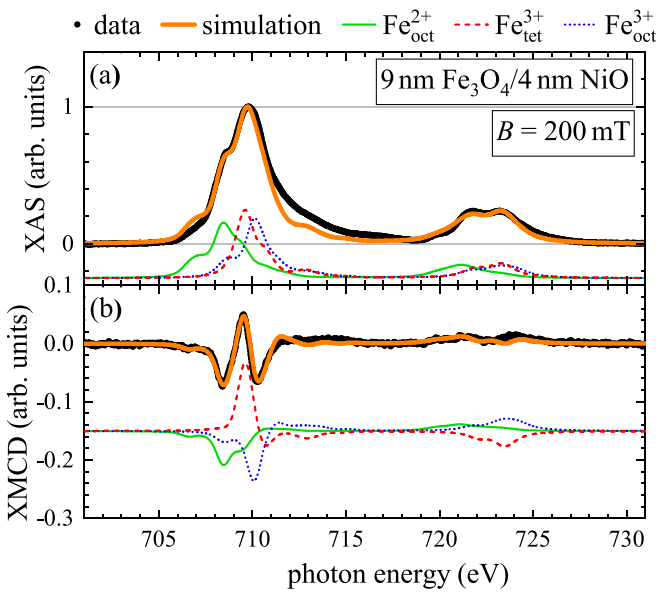

FIG. 2. (a) XAS and (b) XMCD spectrum at the Fe $L_{2,3}$ edges for the Fe_3O_4/NiO/MgO sample, taken at 200 mT external magnetic field, at room temperature and in the TEY mode. A step function was subtracted from the XAS spectrum. Black circles are data points; green, red, and blue spectra are multiplet calculations for the three cation species of Fe_3O_4 assuming an ideal 1 : 1 : 1 stoichiometry; the orange line is their sum. The cation spectra are offset for better visibility.

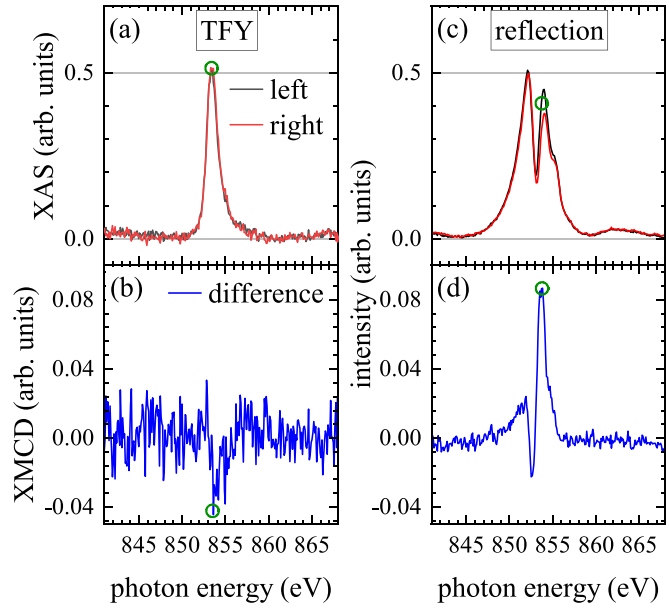

FIG. 3. (a) XAS and (b) XMCD spectra in TFY mode at the Ni L_3 edge for an 18 nm Fe_3O_4/27 nm NiO/MgO sample. (c) Energy scans of the reflected intensity for left and right circularly polarized x rays. (d) Difference of the curves in (c). The green circles indicate the energy at which the XRMR curves were taken (853.6 eV). The XAS data are normalized to the maximum of the XAS spectrum $XAS^{left} + XAS^{right}$. All data are recorded at a fixed incidence glancing angle of 30°.

Ref. [20] as a starting point: We assumed the three-cation model with crystal field energies of $10Dq^{oct} = 1.0$ eV in octahedral and $10Dq^{tet} = -0.6$ eV in tetrahedral coordination. The splittings between the initial and final charge-transfer states were chosen as $\Delta_{init} = 6$ eV and $\Delta_{final} = 5$ eV, and for the exchange splitting, $g \cdot \mu_B = 12 \pm 1$ meV was used. The multiplet states resulting from these calculations were compared to the experimental data by assuming a Gaussian instrumental broadening of 0.25 eV and a Lorentzian lifetime broadening of 0.3 eV at L_3 and 0.6 eV at L_2. Adding the three individual cation spectra with a 1 : 1 : 1 ratio, as expected for Fe_3O_4, results in a total XAS and a total XMCD spectrum [orange lines in Figs. 2(a) and 2(b), respectively], which fit both the XAS and the XMCD data well. The multiplet analysis reveals that at those energies for which the XMCD spectrum has its extrema (708.4, 709.5, 710.2 eV), most of the XMCD signal originates from one dominant cation species [27]. The individual contributions of each cation species to the XMCD spectrum at these three energies can be found in Table II. Therefore, XRMR measurements on those energies are mostly sensitive to one specific cation species. This allows the contributions from the individual cations to the magneto-optical depth profiles to be disentangled.

TABLE II. Contributions of the three cation species to the extrema in the XMCD spectrum in Fig. 2(b) as obtained by the multiplet analysis.

Energy	Fe^{2+}_{oct}	Fe^{3+}_{tet}	Fe^{3+}_{oct}
708.4 eV	70 ± 5%	−8 ± 3%	22 ± 5%
709.5 eV	19 ± 3%	−63 ± 3%	18 ± 3%
710.2 eV	4 ± 2%	−25 ± 8 %	71 ± 10 %

Since the TEY mode has a probing depth of about 3 nm in Fe_3O_4 [28], the TEY signal from the buried NiO film was strongly attenuated at the Ni L_3 edge. For a clearer signal, we brought a 18 nm Fe_3O_4/27 nm NiO/MgO sample to beamline I10 of DLS, and measured XAS and XMCD in the TFY mode at a fixed incident angle of 30°, whose probing depth is only limited by the x-ray attenuation length in Fe_3O_4 of about 80 nm [29] [cf. Figs. 3(a) and 3(b)]. Simultaneously, we measured the reflected intensity in order to obtain an estimate of the magneto-optic effects in reflection [cf. Figs. 3(c) and 3(d)].

B. XRMR

The XRMR data were recorded by measuring XRR curves at resonant energies E_i with extrema in the XMCD signal of Fe_3O_4 [minimum at 708.4 eV, maximum at 709.5 eV, minimum at 710 eV, see Fig. 2(b)] and for NiO [minimum at 853.6 eV, see Fig. 3(b)] with both left and right circularly polarized x rays. Resonant "nondichroic" XRR curves were obtained by averaging the signals I^σ from both helicities (σ = right/left)

$$I = (I^{right} + I^{left})/2, \quad (3)$$

and the XRMR asymmetry ratios by subtracting and normalizing them,

$$\Delta I = \frac{I^{\text{right}} - I^{\text{left}}}{I^{\text{right}} + I^{\text{left}}}. \tag{4}$$

These curves were then fitted with the Zak matrix formalism using the software REMAGX [30] to determine the depth profiles of the complex refractive index $n(z)$,

$$n(z) = 1 - \delta(z) + i\beta(z) \tag{5}$$

along the film height z. The optical dispersion δ and the optical absorption β can be split into nonmagnetic components δ_0, β_0 and magneto-optical components $\Delta\delta$, $\Delta\beta$. In the case of an in-plane magnetic field longitudinal to the x-ray beam as applied here, they can be written as [30]

$$\delta(z) = \delta_0(z) \mp \Delta\delta(z)\cos(\theta), \tag{6}$$

$$\beta(z) = \beta_0(z) \pm \Delta\beta(z)\cos(\theta), \tag{7}$$

for which the magneto-optical contributions depend on the x-ray incidence glancing angle θ and their sign on the helicity of the x rays. The optical absorption β_0 is proportional to the XAS signal, while the magneto-optical absorption $\Delta\beta$ is proportional to the XMCD signal. Thus, $\Delta\beta(z)$ is a measure of the magnetization along the film depth. A detailed review of the XRMR method and the software is given in Ref. [30], and a conclusive recipe for fitting XRMR data can be found in Refs. [31–33].

IV. RESULTS

Figure 3(a) shows the XAS spectra at the Ni L_3 edge of the 18 nm Fe_3O_4/27 nm NiO/MgO sample recorded with left and right circularly polarized x rays in the TFY mode, and Fig. 3(b) shows their difference. The XMCD signal is about 3% of the XAS maximum. In reflection, the magneto-optical effects become even more apparent. Note that the data are recorded at fixed incidence angle of $\theta = 30°$. Therefore the scattering vector q_z changes from 0.426 to 0.440 Å^{-1} along with the energy in the range displayed in Figs. 3(c) and 3(d). At the Ni L_3 resonant energy of 853.6 eV, the magneto-optically induced change of the reflected intensity ranges up to about 8%, demonstrating a strong magneto-optical signal from NiO. This energy was chosen for the XRMR measurements at the Ni L_3 resonance and is indicated by the green circles in Fig. 3.

The data and fits of the resonant XRR measurements, which were obtained by averaging the I^{right} and I^{left} signals, can be found in Fig. 1 alongside the off-resonant XRR curves recorded with 1 keV photons. Figures 4(a) and 4(b) show the XRMR data for the Fe_3O_4/MgO and the Fe_3O_4/NiO/MgO samples at the three Fe L_3 resonant energies 708.4, 709.5, and 710.2 eV, and the Ni L_3 resonant energy 853.6 eV, together with their respective fits, which describe the data very well. The fits in Fig. 4(b) were obtained from the magneto-optical depth profile models which are displayed in Fig. 5(a) for all four resonant energies of the Fe_3O_4/NiO/MgO sample. The gray line represents the optical absorption $\beta_{\text{off-res}}$ obtained from the off-resonant XRR measurement, and represents the structural depth profiles of the sample. It has three plateaus

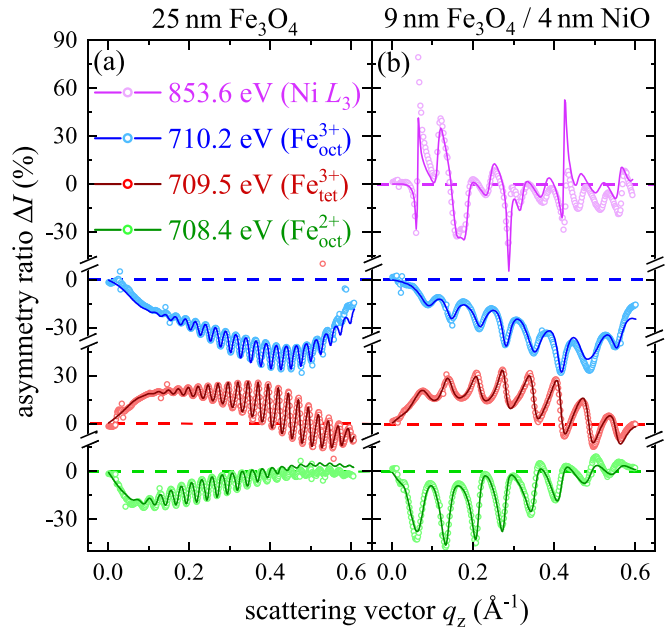

FIG. 4. XRMR data (open circles) and fits (solid lines) from (a) the Fe_3O_4/MgO and (b) the Fe_3O_4/NiO/MgO sample, recorded at the three resonant energies of the Fe XMCD L_3 edge and the Ni L_3 edge. The magneto-optical depth profile models corresponding to the fits in (a) are displayed in Fig. 5(b), and the interface regions of the magneto-optical depth profiles corresponding to the fits in (b) are shown in Fig. 5(c). The q_z range shown corresponds to an angular range of $2\theta = 0°$–$115°$.

corresponding to the MgO substrate, the NiO film, and finally the Fe_3O_4 film, as illustrated by the sketch on top of the panel. An optically thin surface layer of 9 ± 3 Å thickness had to be included, likely stemming from adatoms settling on the surface upon the exposure to air. However, this layer does not contribute to the magnetic signal. The filled areas are the magneto-optical depth profiles $\Delta\beta(z)$ at the resonant energies of the three iron cation species and the Ni L_3 energy, obtained from the XRMR asymmetry ratios.

One notable feature of these magneto-optical depth profiles is found at the surface of the Fe_3O_4 films. Here, a thin layer of enhanced magneto-optical absorption is observed at 709.5 and 710.2 eV, both for the Fe_3O_4/MgO(001) and the Fe_3O_4/NiO/MgO(001) samples. This is likely related to a modification of the cation stoichiometry at the Fe_3O_4(001) surface. This effect is discussed in detail in Ref. [27] for Fe_3O_4/MgO(001), and it is interesting to note that it occurs on the Fe_3O_4/NiO/MgO(001) sample too, as exemplified by Fig. 5(a). However, it is not the subject of the current study, which focuses on the Fe_3O_4/MgO and Fe_3O_4/NiO interfaces.

Therefore, Fig. 5(b) focuses upon the interface region of the magneto-optical depth profiles of the Fe_3O_4/MgO sample, according to the fits in Fig. 4(a). Both the interfaces of the magneto-optical depth profile at 708.4 eV (green) and of the one at 710.2 eV (blue) are collocated with the structural interface (gray line) at $z = 0$ Å. However, the interface of the magneto-optical depth profile at 709.5 eV (red) is shifted by a distance $\Delta z_{709.5\,\text{eV}} = 3.2 \pm 1.3$ Å away from the interface

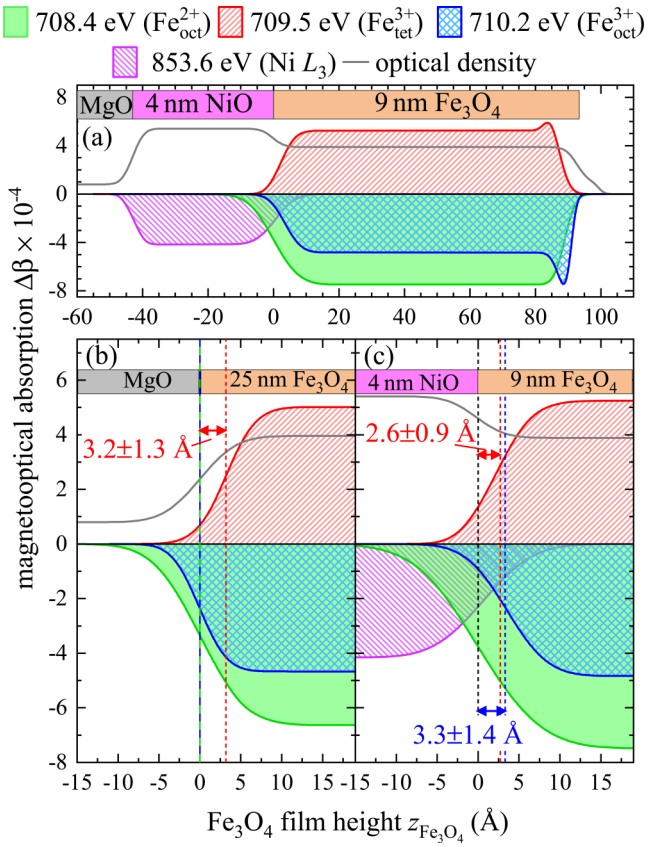

FIG. 5. (a) $\Delta\beta(z)$ depth profiles at the three Fe L_3 resonant energies and the Ni L_3 energy of the Fe_3O_4/NiO/MgO sample, corresponding to the fits in Fig. 4(b). (b) Closeup of the interface region of the Fe_3O_4/MgO film, obtained from the fits in Fig. 4(a). (c) Closeup of the Fe_3O_4/NiO interface region of the magneto-optical depth profiles in (a). The gray lines indicate the optical absorption profiles $\beta_{\text{off-res}}(z)$ obtained by off-resonant XRR fits. Dashed lines highlight the interface positions of the magneto-optical depth profiles.

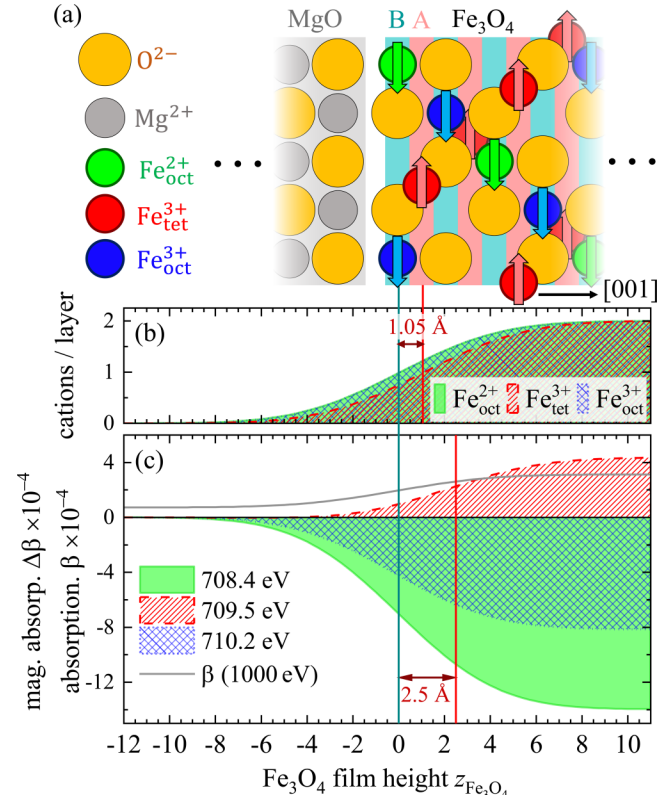

FIG. 6. (a) Illustration of the stacking order at a *B*-terminated Fe_3O_4/MgO(001) interface. The blue and red shaded areas indicate octahedral and tetrahedral layers, respectively. Arrows depict magnetic moments. (b) Simulated cation profiles at the interface of a Fe_3O_4 film with a roughness of $\sigma = 3.5$ Å, in scale with (a). (c) Expected magneto-optical depth profiles at the three resonant energies of the Fe L_3 edge, stemming from the cation profiles in (b), and assuming the magneto-optical absorption contributions of the individual cation spectra presented in Fig. 2(b).

into the Fe_3O_4 film. The roughnesses of the magneto-optical depth profiles at both Fe^{3+} resonances follow the structural depth profile. In contrast, the roughness of the magneto-optical depth profile recorded at the Fe^{2+}_{oct} energy, $\sigma_{708.4\,\text{eV}} = 4.4 \pm 0.2$ Å, is slightly larger than the structural roughness $\sigma_{\text{substrate}} = 3.5 \pm 0.5$ Å.

For the Fe_3O_4/NiO/MgO film, the results are slightly different. Figure 5(c) shows the Fe_3O_4/NiO interface region of the Fe_3O_4/NiO/MgO sample. The XRMR data at the Ni L_3 edge can be well fitted with a homogeneous magnetization profile throughout the NiO film. The interfaces of the magneto-optical depth profiles at the Ni L_3 edge and at the Fe^{2+}_{oct}-related resonance at 708.4 eV are collocated with the structural interface, indicating intact structural and magnetic order for both species. Notably, both their roughnesses are slightly higher, $\sigma_{708.4\,\text{eV}} = 6.3 \pm 0.7$ Å, $\sigma_{853.6\,\text{eV}} = 5.0 \pm 0.7$ Å, compared to the structural roughness $\sigma_{Fe_3O_4/NiO} = 3.0 \pm 0.2$ Å.

In contrast to the magneto-optical depth profile at 708.4 eV, which directly follows the structural profile, the profiles at 709.5 and 710.2 eV are rising with shifts of $\Delta z_{709.5\,\text{eV}} = 2.6 \pm 0.9$ Å and $\Delta z_{710.2\,\text{eV}} = 3.3 \pm 1.4$ Å, respectively, apart from the interface, pointing to a lack of magneto-optical absorption at resonant energies of both Fe^{3+}_{oct} and Fe^{3+}_{tet} at the interface.

V. DISCUSSION

For the Fe_3O_4/MgO sample, it is shown in Fig. 5(b) that the magneto-optical depth profile recorded at a photon energy of 709.5 eV is displaced from the interface into the Fe_3O_4 film by a shift $\Delta z_{709.5\,\text{eV}}$. From the quality of the fits, we can determine this shift to the range $\Delta z_{709.5\,\text{eV}} = 3.2 \pm 1.3$ Å. This result is consistent with a *B*-terminated interface having octahedrally coordinated Fe^{2+} and Fe^{3+} cations in the Fe_3O_4 interface layer. Because about 63% of the magneto-optical contribution at the 709.5 eV resonance stem from the tetrahedrally coordinated iron species Fe^{3+}_{tet}, a lower magneto-optical signal is expected at the interface. Figure 6(a) shows the ideal stacking order at a *B*-terminated Fe_3O_4/MgO(001) interface. The oxygen fcc sublattice of the substrate continues as the oxygen fcc sublattice of the film. In the [001] direction, Fe_3O_4 can be described as a stack of subsequent *B* layers consisting of O^{2-} anions as

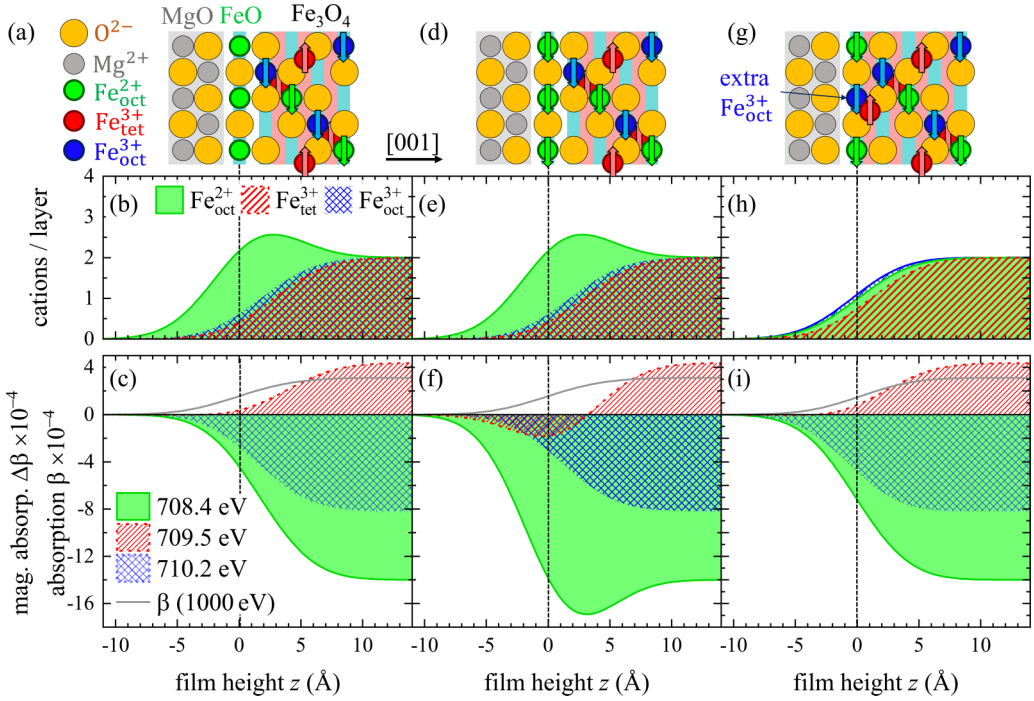

FIG. 7. Simulated magneto-optical depth profiles for three models of the Fe_3O_4/MgO interface. (a), (d), (g) Illustrations of the stacking orders of Fe_3O_4/MgO interfaces (a) with a single nonmagnetic $Fe_{1-\delta}O$ interlayer, (d) with a single ferromagnetic $Fe_{1-\delta}O$ interlayer, and (g) with an additional Fe^{3+}_{oct} cation in the interface layer, following the model of Chang *et al.* [34]. (b), (e), (h) Cation depth profiles corresponding to the illustrations in (a), (d), (g), respectively. (c), (f), (i) Magneto-optical profiles resulting from the cation profiles in (b), (e), (h), respectively. Distances of the rising edges of the magneto-optical profiles from the structural interface can be found in Table III.

well as Fe^{2+}_{oct} and Fe^{3+}_{oct} cations, and *A* layers containing Fe^{3+}_{tet} cations with a distance of 1.05 Å between them. The stacking of *B* and *A* layers is depicted as blue and red shaded areas, respectively, in Fig. 6(a) with the interface layer being a *B* layer (*B* termination). Simulated cation depth profiles following this model are shown in Fig. 6(b). The atomically sharp distributions are smeared out using an interface roughness of $\sigma = 3.5$ Å corresponding to the experimentally determined roughness of the Fe_3O_4/MgO interface. The rising edge of the Fe^{3+}_{tet} depth profile is shifted by $\Delta z_{tet} = 1.05$ Å from the interfaces of the Fe^{2+}_{oct} and Fe^{3+}_{oct} profiles into the Fe_3O_4 film.

Because of the overlap of the individual cation spectra [cf. Fig. 2(b)], the expected magneto-optical depth profiles at the different resonant energies do not follow this behavior exactly. Taking into account the magneto-optical contributions as derived from the multiplet calculations of each cation at each of the three energies, the expected magneto-optical depth profiles of a *B*-terminated Fe_3O_4/MgO(001) interface can be calculated. They are shown in Fig. 6(c). The expected shift of the magneto-optical depth profile at 709.5 eV is $\Delta z_{709.5\,eV} = 2.5$ Å, consistent with the experimental result of $\Delta z_{709.5\,eV} = 3.2 \pm 1.3$ Å. Therefore, the magneto-optical depth profiles indicate a *B*-terminated Fe_3O_4/MgO(001) interface with no interlayer, and evidently, also no magnetic dead layer.

In this scenario, the magnetic order of all three sublattices has bulk properties down to the interface. The simulations of the *B*-terminated interface also predict that the apparent roughness $\sigma_{708.4\,eV}$ of the magneto-optical depth profiles at 708.4 eV appears to be about 0.5 Å larger than the structural profile $\sigma_{substrate}$. This offers an explanation for the slight mismatch of these two roughnesses observed in the experiment. However, while the discrepancy between the model distance and the experimental distance is well within the error range, it is still substantial enough to make a discussion of alternative models worthwhile.

Both the Fe_3O_4/MgO and the Fe_3O_4/NiO interfaces have been studied by various methods. Spintronic devices require interfaces that are structurally, but especially also magnetically sharp. Therefore, focus has been laid on the possible presence of interlayers and intermixing at the interfaces. In the case of Fe_3O_4 directly grown on a substrate, the formation of FeO interlayers has been reported on both metal and oxide substrates [35–37], and particularly on MgO(001) for films deposited at room temperature [13]. The possibility of a single atomic $Fe_{1-\delta}O$ interlayer is discussed in the following. The corresponding magneto-optical depth profiles are calculated in Figs. 7(a)–7(f) for two scenarios.

Therefore, the first reasonable scenario is that the $Fe_{1-\delta}O$ interlayer forms a magnetic dead layer at the interface, presented in Figs. 7(a)–7(c). Figure 7(a) shows an illustration of the stacking order, Fig. 7(b) the cation depth profiles simulated with a roughness of $\sigma = 3.5$ Å, and Fig. 7(c) the resulting magneto-optical depth profiles. $Fe_{1-\delta}O$ is paramagnetic at room temperature. Due to the magnetically dead $Fe_{1-\delta}O$ layer, the rising edges of the magneto-optical depth profiles at both 708.4 and 710.2 eV are shifted about 2 Å into the Fe_3O_4 film compared to the structural interface (cf. Table III), not consistent with the observed profiles in Fig. 5(b).

TABLE III. Distances of the rising edges of the magneto-optical profiles from the structural interface at the three resonant energies. Considered here are the results from the two investigated samples as well as the discussed interface models: the *B*-terminated model (cf. Fig. 6), the nonmagnetic (NM) $Fe_{1-\delta}$ interface layer [cf. Figs. 7(a)–7(c)], the ferromagnetic (FM) $Fe_{1-\delta}$ interface layer [cf. Figs. 7(d)–7(f)], and the model proposed by Chang *et al.* [34] [cf. Figs. 7(g)–7(i)].

	Fe_3O_4/MgO	Fe_3O_4/NiO/MgO	*B*-term.	$Fe_{1-\delta}$ (NM)	$Fe_{1-\delta}$ (FM)	Chang
$\Delta z_{708.4\,\mathrm{eV}}$ (Å)	0	0	0	1.7	0	0
$\Delta z_{709.5\,\mathrm{eV}}$ (Å)	3.2 ± 1.3	2.6 ± 0.9	2.5	4.1	5.5	2.5
$\Delta z_{710.2\,\mathrm{eV}}$ (Å)	0	3.3 ± 1.4	0	1.7	1.1	−0.5

The second scenario assumes that the very thin FeO layer magnetically couples to Fe_3O_4 and the magnetic order of its Fe^{2+}_{oct} sublattice is extended into the FeO layer. The resulting magneto-optical depth profiles show nonmonotonic behavior and differ even more from the observed ones [cf. Figs. 7(d)–7(f) and Table III].

Our data therefore do not indicate any magnetically dead layers, which had been considered to be the cause of the magnetization reduction in Fe_3O_4 ultrathin films [14,34,38], nor interlayers of ferromagnetic FeO. Since it has already been shown that the magneto-optical depth profiles can be explained without an interlayer, it is unlikely that a FeO interlayer of more than a single atomic layer is present.

Another interesting model, which was proposed by Chang *et al.* for the growth dynamics of Fe_3O_4 [34], shall also briefly be mentioned here. This model suggests the first interface *B* layer to contain one additional Fe^{3+}_{oct} cation per unit formula $[(Fe^{2+}_{oct})_2(Fe^{3+}_{oct})_3O_8$ instead of $(Fe^{2+}_{oct})_2(Fe^{3+}_{oct})_2O_8]$. An illustration can be seen in Fig. 7(g). Both the cation depth profiles and the simulated magneto-optical depth profiles resulting from this model, presented in Figs. 7(h) and 7(i), hardly differ from the *B*-terminated interface shown in Figs. 6(b) and 6(c). Although XRMR would in principle be an ideal method to test this model, the lacking spatial resolution in our experiments can neither confirm nor reject a faint phenomenon such as an additional Fe^{3+}_{oct} cation in the interface layer.

For the Fe_3O_4/NiO/MgO(001) sample, a noteworthy finding is the dichroic signal of the NiO film. Bulk NiO is an antiferromagnet at room temperature and should not show any circular dichroism. However, as demonstrated in Fig. 3, we clearly observe magneto-optical effects in both the TFY mode and in reflection at the Ni L_3 edge. Interestingly, we can exclude the XMCD signal to stem from uncompensated surface spins, since the magneto-optical depth profiles clearly show a homogeneous magnetization of the entire film. Size effects of the magnetic properties of NiO and related antiferromagnets, including ferromagnetic behavior at room temperature, have been frequently reported before, mostly for NiO nanoparticles, but also CoO thin-film systems [39–44]. Another possible explanation for the XMCD and asymmetry signals of NiO is offered by a canting of the magnetic moments in NiO. For Fe_3O_4/NiO ultrathin films, a spin-flop coupling of NiO to the Fe_3O_4(001) interface has been reported [19]. In that case, the antiferromagnetic order of NiO aligns perpendicular to the magnetization of Fe_3O_4, but with a small canting of the Ni^{2+} moments, resulting in a magnetization component parallel to the ferrimagnet. This reaction of NiO to outer magnetic fields has also been confirmed by spin Hall magnetoresistance measurements [45–47]. The mechanism can be summarized as follows [48]: A superexchange field $H_e = 968$ T [49,50] mediated by the O^{2-} anions causes neighboring (111) planes in NiO to align antiparallel. If an outer magnetic field H is applied, the magnetic sublattices are canted by a small angle $\theta = \arcsin(H/2H_e) \ll 1^\circ$ in order to gain Zeeman energy. As soon as the Zeeman energy becomes comparable to the magnetic anisotropy energy, the moments can align to the magnetic field. While this is an established effect in NiO, the size of the magneto-optic response stemming from NiO is remarkably large, in the same range as that of Fe_3O_4. However, conversion factors from $\Delta\beta$ to μ_B/atom can be of quite different size as recently observed for Pt and Pd [51,52]. The determination of this conversion factor for NiO is beyond the scope of this work and will be the focus of future research. Nevertheless, the Fe_3O_4/NiO interface and its magnetic depth profile obtained by XRMR should still be reported here due to the importance for spintronic applications.

The interface of Fe_3O_4/NiO has mostly been discussed regarding the presence of a $NiFe_2O_4$ interlayer. In reports by Gatel *et al.* [18] and Pilard *et al.* [53], high-resolution transmission electron microscopy (HRTEM) images show generally sharp interfaces between the rocksalt structure of NiO and the spinel structure of Fe_3O_4. However, this only partly solves the question, because the lack of chemical and magnetic contrast cannot exclude, for instance, the formation of a rocksalt (Fe, Ni)O phase or a spinel $NiFe_2O_4$ phase. Gatel *et al.* addressed this issue by performing both HRTEM and electron energy loss spectroscopy (EELS) [18]. For a NiO/Fe_3O_4/MgO(001) sample, for which the NiO film was deposited at a substrate temperature of 700 °C, indeed an intermediate $NiFe_2O_4$ phase was observed. For a Fe_3O_4/NiO/MgO(001) stack, which had the Fe_3O_4 film deposited at 400 °C, the interface appeared to be chemically sharp with at most minor interdiffusion [18]. The $NiFe_2O_4$ phase they observe in the NiO/Fe_3O_4/MgO(001) stack is likely caused by thermal interdiffusion due to the high deposition temperature [10].

A formation of a well-ordered $NiFe_2O_4$ interlayer does not match our observations. $NiFe_2O_4$ crystallizes in the same inverse spinel structure as Fe_3O_4, but with Ni^{2+}_{oct} cations instead of Fe^{2+}_{oct} sharing the *B* sites with Fe^{3+}_{oct}. Analogous to Fe_3O_4, the magnetic moments of the Ni^{2+}_{oct} and Fe^{3+}_{oct} cations on the *B* sites align antiferromagnetically to the magnetic moments of the Fe^{3+}_{tet} cations on the *A* sites. For the magneto-optical depth profiles, this would imply a decrease of Fe^{2+}_{oct} cations close to the interface and thus of the magneto-optical absorption at 708.4 eV, while the magneto-optical absorption depth profiles for 709.5 and 710.2 eV should stay constant in a $NiFe_2O_4$

layer. Instead, we observe a reduction of the magneto-optical absorption at 709.5 and 710.2 eV as compared to the case of the Fe_3O_4/MgO interface. This behavior, together with the increased roughnesses of the magneto-optical depth profiles at the Fe^{2+}_{oct} and the Ni^{2+} energies, might indicate a slight intermixing of Fe^{2+}_{oct} into the rocksalt structure of NiO. However, this effect may not extend farther than a single atomic layer. Notably, the ferromagnetic coupling between the Fe^{2+}_{oct} cations is retained down to the interface regardless of the intermixing.

VI. CONCLUSION

We have prepared ultrathin Fe_3O_4/MgO(001) and Fe_3O_4/NiO/MgO(001) films by RMBE and performed XMCD and XRMR measurements to extract magneto-optical depth profiles for the individual cation species Fe^{2+}_{oct}, Fe^{3+}_{tet}, and Fe^{3+}_{oct}, as well as for Ni^{2+}_{oct}. These magneto-optical depth profiles show that for Fe_3O_4/MgO(001), the magnetic order of all three cation species is stable for the entire film with no interlayer or magnetic dead layer at the interface. For Fe_3O_4/NiO films, we observe a dichroic response at the Ni L_3 edge in the NiO film which might be explained by uncompensated magnetic moments throughout the entire NiO film. The magneto-optical profiles of the iron cations reveal an intact magnetic order for the Fe^{2+}_{oct} cation species down to the interface, while the magneto-optical depth profiles at the Fe^{3+}_{oct} and the Fe^{3+}_{tet} resonances are shifted about 3 Å into the Fe_3O_4 film, possibly indicating a single intermixed layer containing both Fe^{2+} and Ni^{2+} cations.

ACKNOWLEDGMENTS

Financial support from the Bundesministerium für Bildung und Forschung (FKZ 05K16MP1) is gratefully acknowledged. We are also grateful for the kind support from the Deutsche Forschungsgemeinschaft (DFG under No. KU 2321/6-1, and No. WO 533/20-1). The authors would like to thank Diamond Light Source for beamtime (Proposal No. SI19173-1), and the staff of beamline I10 for assistance with data collection. We thank HZB for the allocation of synchrotron beamtime at beamline UE46_PGM-1 (181/06266ST/R) where we recorded the XRMR and XMCD measurements.

[1] P. Weiss and R. Forrer, Ann. Phys. **10**, 279 (1929).
[2] J.-B. Moussy, J. Phys. D: Appl. Phys. **46**, 143001 (2013).
[3] J. M. D. Coey and C. L. Chien, MRS Bull. **28**, 720 (2003).
[4] M. Bibes and A. Barthelémy, IEEE Trans. Electron Devices **54**, 1003 (2007).
[5] I. Žutić, J. Fabian, and S. D. Sarma, Rev. Mod. Phys. **76**, 323 (2004).
[6] J. A. Moyer, R. Gao, P. Schiffer, and L. W. Martin, Sci. Rep. **5**, 10363 (2015).
[7] L. Marnitz, K. Rott, S. Niehörster, C. Klewe, D. Meier, S. Fabretti, M. Witziok, A. Krampf, O. Kuschel, T. Schemme, K. Kuepper, J. Wollschläger, A. Thomas, G. Reiss, and T. Kuschel, AIP Adv. **5**, 047103 (2015).
[8] N.-T. Kim-Ngan, A. Balogh, J. Meyer, J. Brötz, M. Zajac, T. Ślezak, and J. Korecki, Surf. Sci. **603**, 1175 (2009).
[9] R. F. C. Farrow, M. J. Carey, R. F. Marks, P. M. Rice, and D. J. Smith, Appl. Phys. Lett. **77**, 1191 (2000).
[10] O. Kuschel, R. Buß, W. Spiess, T. Schemme, J. Wöllermann, K. Balinski, A. T. N'Diaye, T. Kuschel, J. Wollschläger, and K. Kuepper, Phys. Rev. B **94**, 094423 (2016).
[11] J. Rodewald, J. Thien, T. Pohlmann, M. Hoppe, F. Timmer, F. Bertram, K. Kuepper, and J. Wollschläger, Phys. Rev. B **100**, 155418 (2019).
[12] F. Bertram, C. Deiter, K. Pflaum, M. Suendorf, C. Otte, and J. Wollschläger, J. Appl. Phys. **110**, 102208 (2011).
[13] F. Bertram, C. Deiter, O. Hoefert, T. Schemme, F. Timmer, M. Suendorf, B. Zimmermann, and J. Wollschläger, J. Phys. D: Appl. Phys. **45**, 395302 (2012).
[14] P. van der Heijden, P. Bloemen, J. Gaines, J. van Eemeren, R. Wolf, P. van der Zaag, and W. de Jonge, J. Magn. Magn. Mater. **159**, L293 (1996).
[15] P. van der Zaag, P. Bloemen, J. Gaines, R. Wolf, P. van der Heijden, R. van de Veerdonk, and W. de Jonge, J. Magn. Magn. Mater. **211**, 301 (2000).
[16] T. Kado, Appl. Phys. Lett. **92**, 092502 (2008).
[17] J. Keller, P. Miltényi, B. Beschoten, G. Güntherodt, U. Nowak, and K. D. Usadel, Phys. Rev. B **66**, 014431 (2002).
[18] C. Gatel, E. Snoeck, V. Serin, and A. Fert, Eur. Phys. J. B **45**, 157 (2005).
[19] I. P. Krug, F. U. Hillebrecht, M. W. Haverkort, A. Tanaka, L. H. Tjeng, H. Gomonay, A. Fraile-Rodríguez, F. Nolting, S. Cramm, and C. M. Schneider, Phys. Rev. B **78**, 064427 (2008).
[20] K. Kuepper, O. Kuschel, N. Pathé, T. Schemme, J. Schmalhorst, A. Thomas, E. Arenholz, M. Gorgoi, R. Ovsyannikov, S. Bartkowski, G. Reiss, and J. Wollschläger, Phys. Rev. B **94**, 024401 (2016).
[21] G. Mariotto, S. Murphy, and I. V. Shvets, Phys. Rev. B **66**, 245426 (2002).
[22] R. Bliem, E. McDermott, P. Ferstl, M. Setvin, O. Gamba, J. Pavelec, M. A. Schneider, M. Schmid, U. Diebold, P. Blaha, L. Hammer, and G. S. Parkinson, Science **346**, 1215 (2014).
[23] E. Weschke and E. Schierle, J. Large-Scale Res. Facil. **4**, A127 (2018).
[24] G. van der Laan, J. Electron Spectrosc. Relat. Phenom. **86**, 41 (1997).
[25] F. de Groot, Coord. Chem. Rev. **249**, 31 (2005).
[26] E. Stavitski and F. M. de Groot, Micron **41**, 687 (2010).
[27] T. Pohlmann, T. Kuschel, J. Rodewald, J. Thien, K. Ruwisch, F. Bertram, E. Weschke, P. Shafer, J. Wollschläger, and K. Küpper, Phys. Rev. B **102**, 220411(R) (2020).
[28] G. F. M. Gomes, T. E. P. Bueno, D. E. Parreiras, G. J. P. Abreu, A. de Siervo, J. C. Cezar, H.-D. Pfannes, and R. Paniago, Phys. Rev. B **90**, 134422 (2014).
[29] B. Henke, E. Gullikson, and J. Davis, At. Data Nucl. Data Tables **54**, 181 (1993).
[30] S. Macke and E. Goering, J. Phys.: Condens. Matter **26**, 363201 (2014).
[31] T. Kuschel, C. Klewe, J.-M. Schmalhorst, F. Bertram, O. Kuschel, T. Schemme, J. Wollschläger, S. Francoual, J. Strempfer, A. Gupta, M. Meinert, G. Götz, D. Meier, and G. Reiss, Phys. Rev. Lett. **115**, 097401 (2015).

[32] C. Klewe, T. Kuschel, J.-M. Schmalhorst, F. Bertram, O. Kuschel, J. Wollschläger, J. Strempfer, M. Meinert, and G. Reiss, Phys. Rev. B **93**, 214440 (2016).
[33] J. Krieft, D. Graulich, A. Moskaltsova, L. Bouchenoire, S. Francoual, and T. Kuschel, J. Phys. D: Appl. Phys. **53**, 375004 (2020).
[34] C. F. Chang, Z. Hu, S. Klein, X. H. Liu, R. Sutarto, A. Tanaka, J. C. Cezar, N. B. Brookes, H.-J. Lin, H. H. Hsieh, C. T. Chen, A. D. Rata, and L. H. Tjeng, Phys. Rev. X **6**, 041011 (2016).
[35] S. Gota, E. Guiot, M. Henriot, and M. Gautier-Soyer, Phys. Rev. B **60**, 14387 (1999).
[36] J. Karunamuni, R. L. Kurtz, and R. L. Stockbauer, Surf. Sci. **442**, 223 (1999).
[37] C. Schlueter, M. Lübbe, A. Gigler, and W. Moritz, Surf. Sci. **605**, 1986 (2011).
[38] Y. Zhou, C. McEvoy, R. Ramos, and I. V. Shvets, J. Appl. Phys. **99**, 08J111 (2006).
[39] T. Ambrose and C. L. Chien, Phys. Rev. Lett. **76**, 1743 (1996).
[40] R. H. Kodama, S. A. Makhlouf, and A. E. Berkowitz, Phys. Rev. Lett. **79**, 1393 (1997).
[41] E. Winkler, R. D. Zysler, M. Vasquez Mansilla, and D. Fiorani, Phys. Rev. B **72**, 132409 (2005).
[42] L. Li, L. Chen, R. Qihe, and G. Li, Appl. Phys. Lett. **89**, 134102 (2006).
[43] P. Ravikumar, B. Kisan, and A. Perumal, AIP Adv. **5**, 087116 (2015).
[44] N. Rinaldi-Montes, P. Gorria, D. Martínez-Blanco, A. B. Fuertes, I. Puente-Orench, L. Olivi, and J. A. Blanco, AIP Adv. **6**, 056104 (2016).
[45] D. Hou, Z. Qiu, J. Barker, K. Sato, K. Yamamoto, S. Vélez, J. M. Gomez-Perez, L. E. Hueso, F. Casanova, and E. Saitoh, Phys. Rev. Lett. **118**, 147202 (2017).
[46] G. R. Hoogeboom, A. Aqeel, T. Kuschel, T. T. M. Palstra, and B. J. van Wees, Appl. Phys. Lett. **111**, 052409 (2017).
[47] J. Fischer, O. Gomonay, R. Schlitz, K. Ganzhorn, N. Vlietstra, M. Althammer, H. Huebl, M. Opel, R. Gross, S. T. B. Goennenwein, and S. Geprägs, Phys. Rev. B **97**, 014417 (2018).
[48] G. R. Hoogeboom, G.-J. N. S. Nicolaas, A. Alexander, O. Kuschel, J. Wollschläger, I. Ennen, B. J. van Wees, and T. Kuschel, Phys. Rev. B **103**, 144406 (2021).
[49] M. T. Hutchings and E. J. Samuelsen, Phys. Rev. B **6**, 3447 (1972).
[50] S. M. Rezende, A. Azevedo, and R. L. Rodríguez-Suárez, J. Appl. Phys. **126**, 151101 (2019).
[51] D. Graulich, J. Krieft, A. Moskaltsova, J. Demir, T. Peters, T. Pohlmann, F. Bertram, J. Wollschläger, J. R. L. Mardegan, S. Francoual, and T. Kuschel, Appl. Phys. Lett. **118**, 012407 (2021).
[52] D. Graulich and T. Kuschel (private communication).
[53] M. Pilard, O. Ersen, S. Cherifi, B. Carvello, L. Roiban, B. Muller, F. Scheurer, L. Ranno, and C. Boeglin, Phys. Rev. B **76**, 214436 (2007).